Chapter 2
Electromagnetic Eigenmode Simulations of the Third Harmonic Cavity

In order to study the nature of the HOMs in third harmonic cavities present in ACC39, eigenmode simulations have been conducted. This is essential and the first step of searching suitable modes for beam position diagnostics. Eigenmodes of an ideal third harmonic 9-cell cavity are used to study the modal structure of each band and to interpret the HOM spectra measurements described in Chap. 3.

In this chapter, the third harmonic cavity is first treated as a periodic structure with an infinite number of repetitions of the mid-cell. The dispersion curves of monopole, dipole, quadrupole and sextupole passbands are described in Sect. 2.1. The beam pipes connecting cavities modeled as circular waveguides are described in Sect. 2.2. The eigenmodes obtained for an ideal third harmonic cavity without couplers are presented in Sect. 2.3.

2.1 The Third Harmonic Cavity as a Periodic Structure

A sketch of the cell geometry of the third harmonic cavity is given in Fig. 2.1. The cell is rotationally symmetric around the z axis. The iris and the equator both have an elliptical shape. The mid-cell has a different shape compared to the end-cell, and parameters are listed in Table 2.1. The iris of the end-cup is larger than that of the mid-cup in order to accomplish a better coupling [1].

A mid-cell subjected to infinite periodic boundary conditions was simulated. Fig. 2.2a shows a mid-cell modeled in CST Microwave Studio® [2]. A hexahedral mesh was used in the calculation of the electromagnetic field as shown in Fig. 2.2b. The mesh lines were chosen such that the iris radius and the equator radius were exactly matched by mesh lines. Symmetry planes were applied on the structure to save simulation time so that only a quarter of the structure was used (see the region with mesh lines in Fig. 2.2b). Approximately 130,000 mesh cells for a quarter of the structure and a maximum mesh step of 0.85 m were set. Electric (EE) boundary conditions were used on the surface of the mid-cell, while periodic boundary conditions were set on both ends of the cell. A solver accuracy of 10^{-6} in terms of the eigensystem's relative residual was used.

P. Zhang, *Beam Diagnostics in Superconducting Accelerating Cavities*,
Springer Theses, DOI: 10.1007/978-3-319-00759-5_2,

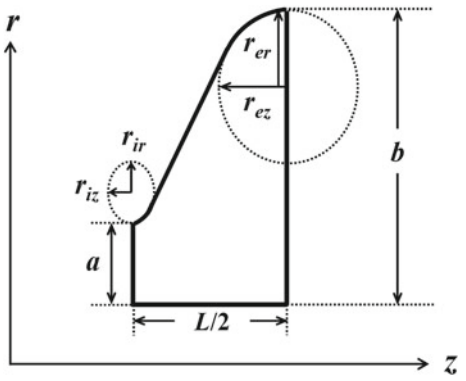

Fig. 2.1 Parameterization of the cell geometry [1]. The *solid curve* represents the cell wall

Table 2.1 Parameters of the cell geometry of the third harmonic cavity [1]

		mid-cup	end-cup
Iris radius, a	mm	15.0	20.0
Equator radius, b	mm	35.787	35.787
Half cell length, $L/2$	mm	19.2167	19.2167
Equator horizontal axis, r_{ez}	mm	13.6	14.4
Equator vertical axis, r_{er}	mm	15.0	15.0
Iris horizontal axis, r_{iz}	mm	4.5	4.5
Iris vertical axis, r_{ir}	mm	6.0	6.0

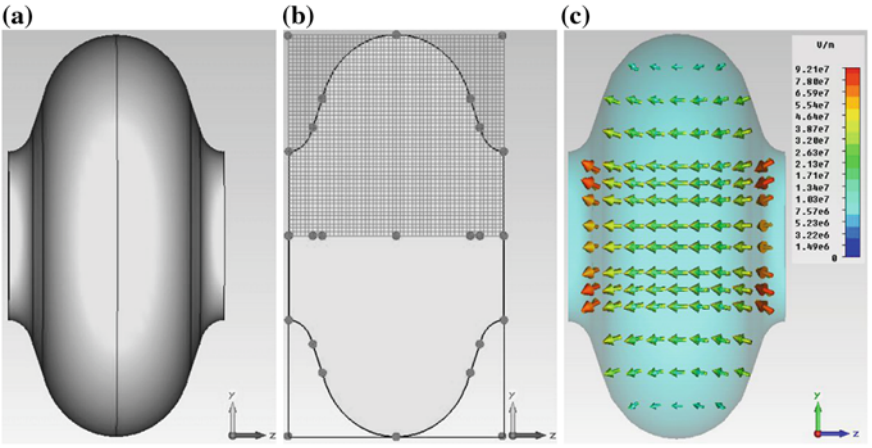

Fig. 2.2 **a**, **b** The mid-cell of the third harmonic cavity as modeled in CST Microwave Studio®. **c** The electric field of the accelerating mode with a phase advance of 180 degrees per cell (π mode)

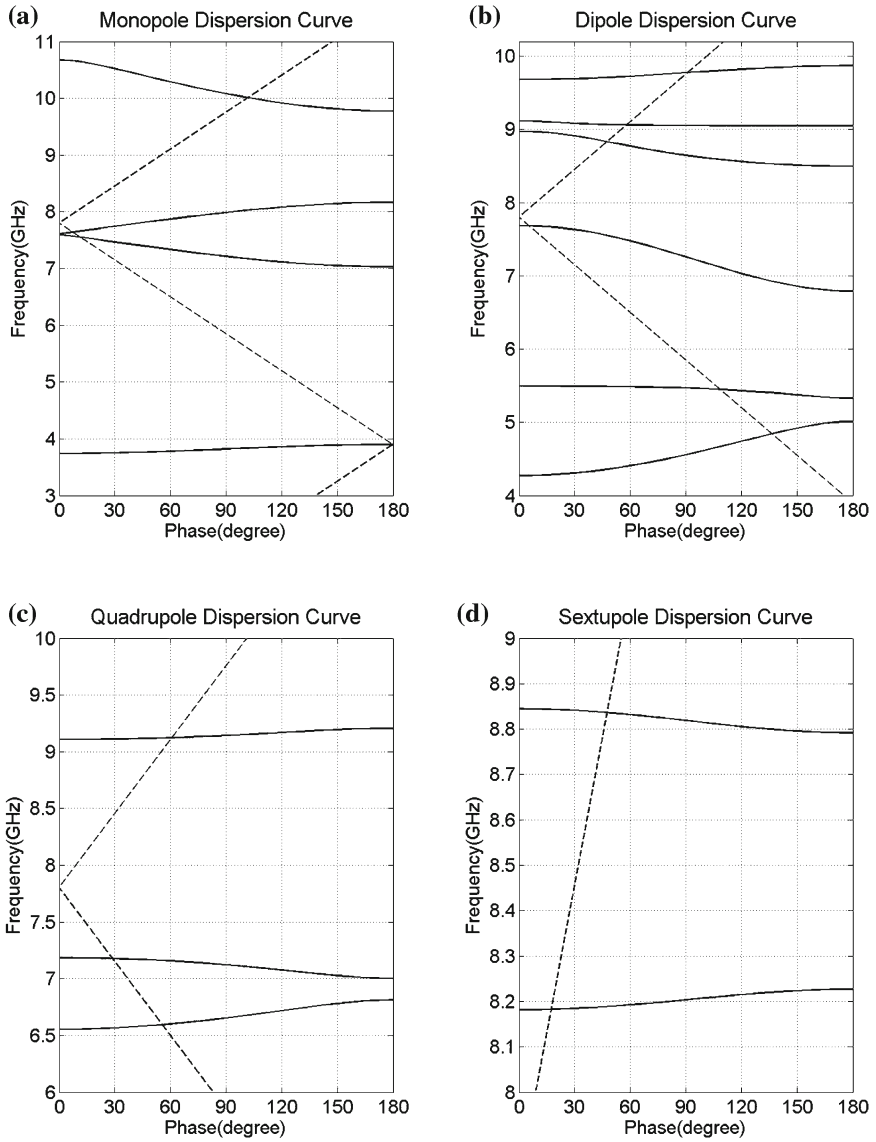

Fig. 2.3 The band structure (*solid curve*) of a 3.9 GHz cavity mid-cell. The light line is *dashed*

The modes of an infinitely long periodic chain of cavities can be obtained from single cell calculations using Floquet periodic boundary conditions:

$$\mathbf{E}(r, z + L) = \mathbf{E}(r, z)e^{i\phi}, \tag{2.1}$$

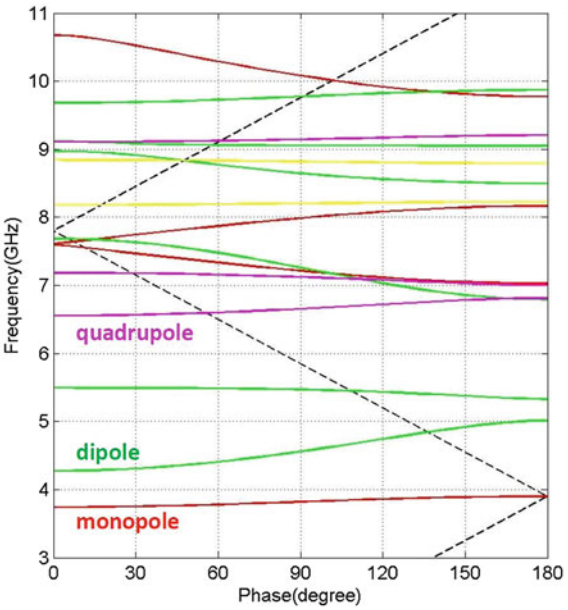

Fig. 2.4 Dispersion curve for monopole (*red*), dipole (*green*), quadrupole (*magenta*) and sextupole (*yellow*) modes. The light line is *dashed*

Table 2.2 Values of p_{mn} and p'_{mn} [3, 4]

	p_{mn} (TM modes)				p'_{mn} (TE modes)		
	m	n = 1	n = 2	n = 3	n = 1	n = 2	n = 3
Monopole	0	**2.405**	5.520	8.654	3.832	7.016	10.174
Dipole	1	3.832	7.016	10.174	**1.841**	5.331	8.536
Quadrupole	2	5.136	8.417	11.620	3.054	6.706	9.970
Sextupole	3	6.380	9.761	13.015	4.201	8.015	11.346

Table 2.3 Cutoff frequencies for the lowest order TE and TM modes in a circular waveguide with a radius of 15 and 20 mm

	a = 15 mm (GHz)	**a** = 20 mm (GHz)
f_c (TE_{11})	5.86	4.39
f_c (TM_{01})	7.65	5.74

where L is the cell length and ϕ is the phase advance per cell. Figure 2.2c shows the electric field of a mode with a phase advance of 180 degrees per cell, which is the so-called π mode. The frequencies of several passbands are shown in the form of dispersion curves [3] in Fig. 2.3 for monopole, dipole, quadrupole and sextupole modes. The phase velocity is defined as [3]

$$v_{phase} = \frac{\omega}{k_z} = 2\pi L \frac{f}{\phi}, \tag{2.2}$$

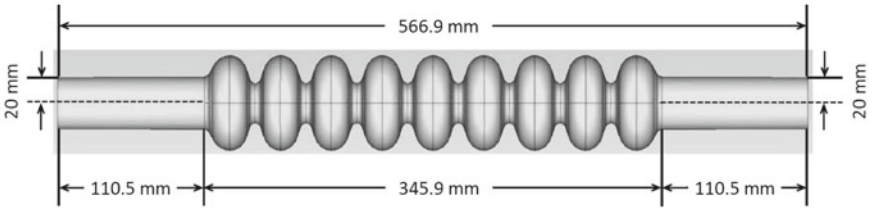

Fig. 2.5 CST Microwave Studio® generated geometry of the third harmonic cavity

Fig. 2.6 A typical mesh used for selected cells in the third harmonic cavity

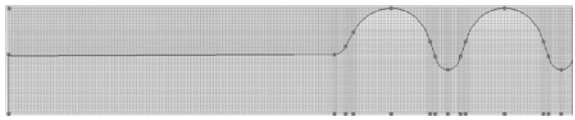

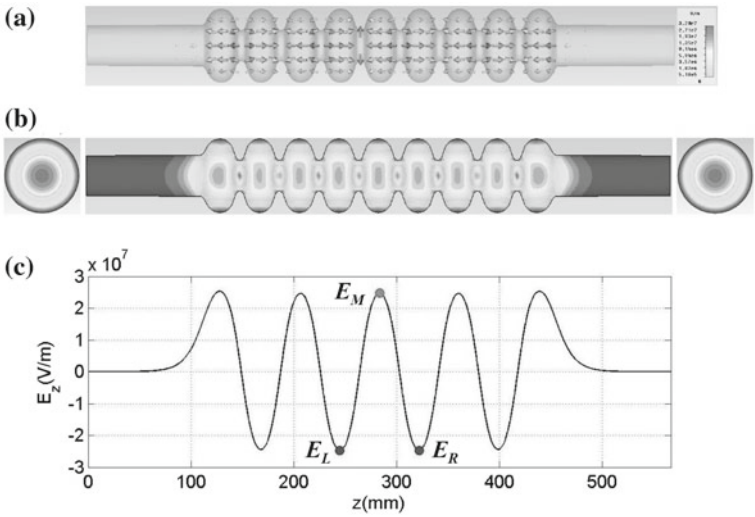

Fig. 2.7 **a** The electric field (*arrows*) of the accelerating mode (3.9 GHz) in the third harmonic cavity. **b** The electric field magnitude of the accelerating mode (frequency: 3.9008 GHz, R/Q: 373.113 Ω). Electric (EE) boundary conditions were used in the simulation. **c** Longitudinal electric field E_z of the accelerating mode (3.9 GHz, π mode) on the cavity axis. The *dots* are corresponding to the position marked in Fig. 2.8 for E_L, E_M and E_R respectively

where k_z is the longitudinal wave number, $\phi = k_z L$ is the phase advance per cell, which is used as a horizontal axis in the plots of the dispersion curves. The phase velocity can be obtained from the dispersion curves using Eq. 2.2.

A beam excites strongest those modes which are synchronous to the beam, i.e. with a phase velocity equal to the speed of the accelerated particles. For FLASH, this is the speed of light, $v_{phase} = c$. The so-called light line can therefore be drawn as the straight line:

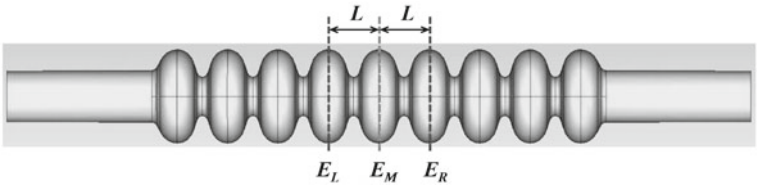

Fig. 2.8 Calculation of the phase advance per cell. E_L, E_M and E_R are longitudinal electric field at certain positions

$$f(\phi) = \frac{c}{2\pi L}\phi. \tag{2.3}$$

It is folded into the phase range from 0 to 180 degrees in the dispersion plots due to the periodicity of the structure. By design, the light line intersects the π mode of the first monopole passband (frequency ≈ 3.9 GHz), which is used for particle acceleration. Figure 2.4 summarizes the calculated dispersion curves for the monopole, dipole, quadrupole and sextupole bands.

2.2 The Beam Pipe as a Circular Waveguide

The third harmonic cavities are connected with beam pipes, whose radius is equal to the iris of the end-cup. To study the propagation of modes amongst cavities, the beam pipes are treated as infinitely long circular waveguides, which can be characterized analytically. Generally, the transverse electric (TE) and transverse magnetic (TM) modes can be distinguished from the characterization of the electric and magnetic fields [3]. The cutoff frequencies of TE and TM modes for a circular waveguide are [4]:

$$f_c(\mathrm{TM_{mn}}) = c\frac{p_{mn}}{2\pi a}, \tag{2.4a}$$

$$f_c(\mathrm{TE_{mn}}) = c\frac{p'_{mn}}{2\pi a}, \tag{2.4b}$$

where $m = 0, 1, 2, 3$ corresponds to monopole, dipole, quadrupole and sextupole modes, p_{mn} is the n^{th} root of the m^{th} Bessel function J_m, p'_{mn} is the n^{th} root of the derivative of the m^{th} Bessel function J'_m, a is the radius of the waveguide. The first TE mode to propagate is the mode with the smallest p'_{mn}, which from Table 2.2 is seen to be $\mathrm{TE_{11}}$ mode. The first TM mode to propagate is then the $\mathrm{TM_{01}}$ mode. The definition of TE_{mn} and TM_{mn} mode can be found in [3]. The cutoff frequencies of $\mathrm{TE_{11}}$ and $\mathrm{TM_{01}}$ modes are listed in Table 2.3 for a circular waveguide with a radius of 15 and of 20 mm. For the third harmonic cavity, 15 mm is the iris radius of a mid-cell, while 20 mm is the iris radius of an end-cup and the radius of connecting

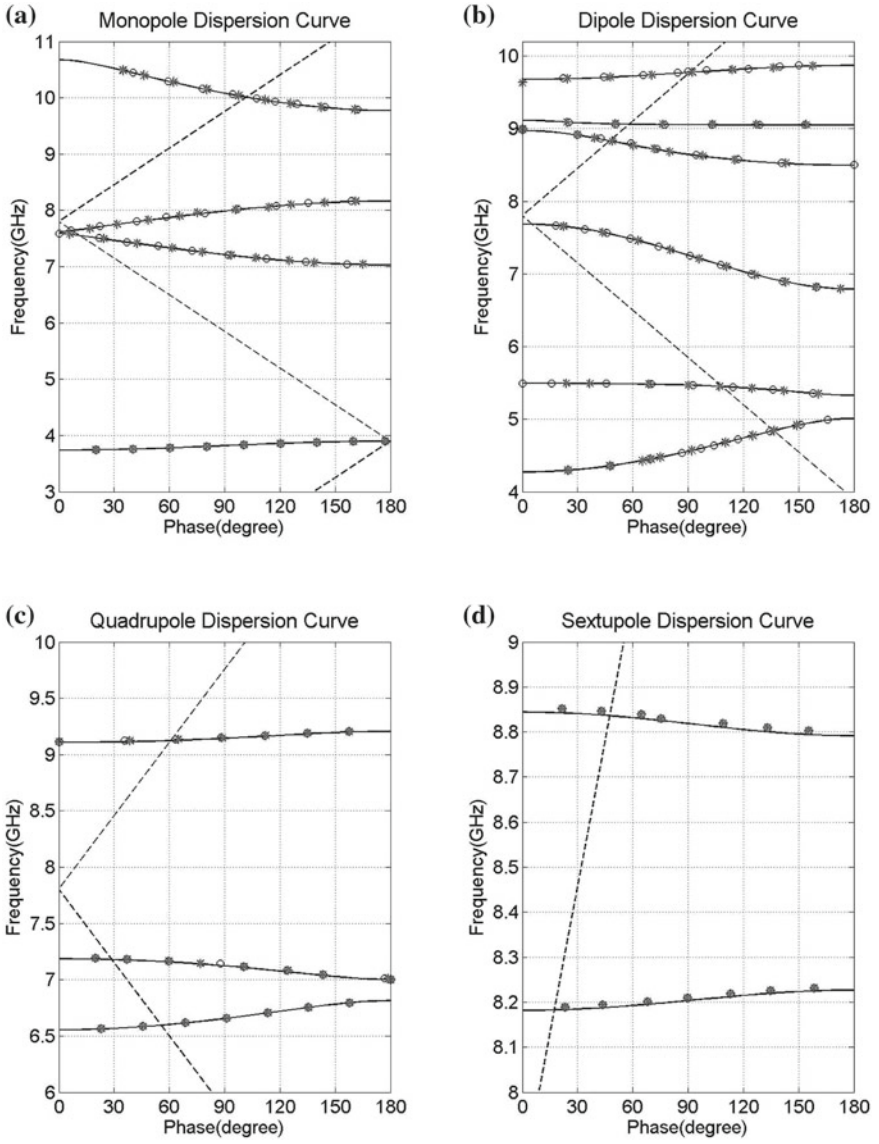

Fig. 2.9 Monopole, dipole, quadrupole and sextupole band structure (*solid curve*) of a mid-cell with periodic boundaries and the modes in an ideal 9-cell 3.9 GHz cavity. The *circles* represent modes calculated with electric (EE) boundary conditions and the *asterisks* represent magnetic (MM) boundary conditions. The light line is *dashed*

beam pipes (see Table 2.1). By choosing a beam-pipe radius larger than 1/3 of that of the 1.3 GHz cavity, the cutoff frequency is lowered so that most higher order modes propagate amongst cavities and are therefore better damped [5].

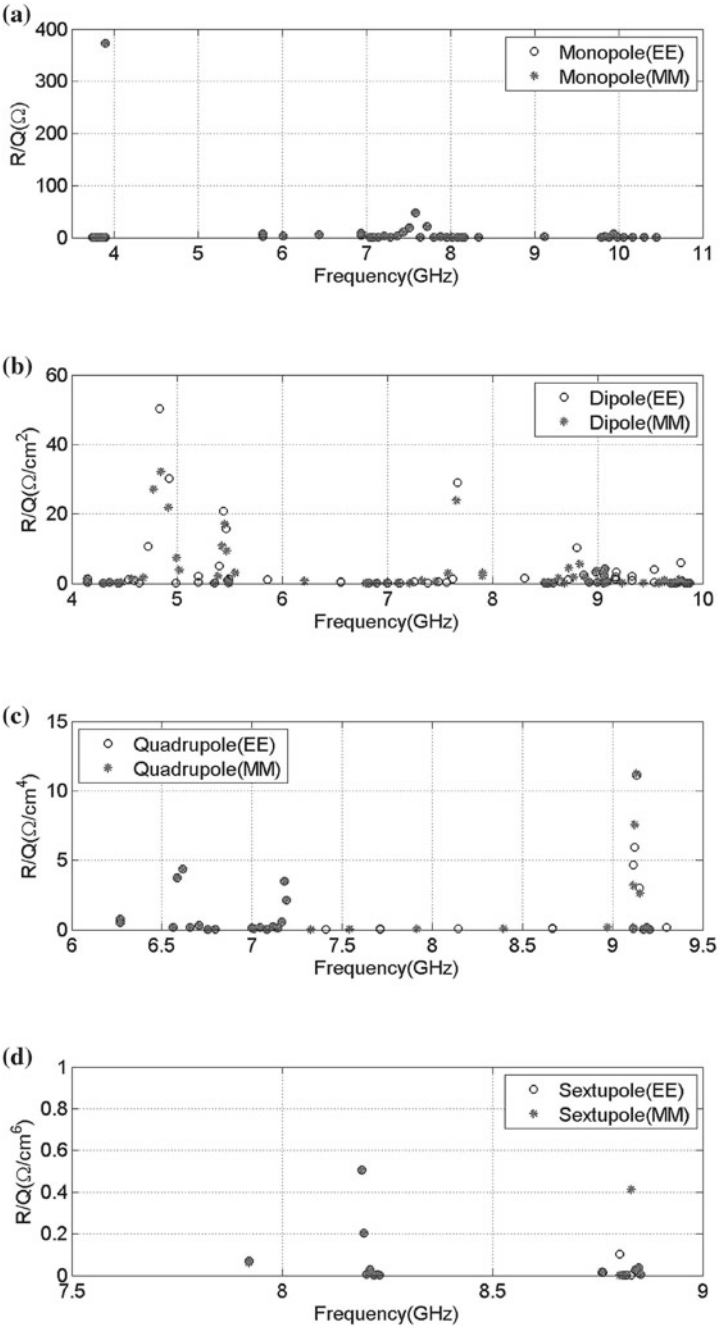

Fig. 2.10 The R/Q parameters of eigenmodes of a 9-cell third harmonic cavity versus the modal frequencies. *Circles* represent modes calculated with electric (EE) boundaries and *asterisks* with magnetic (MM) boundaries

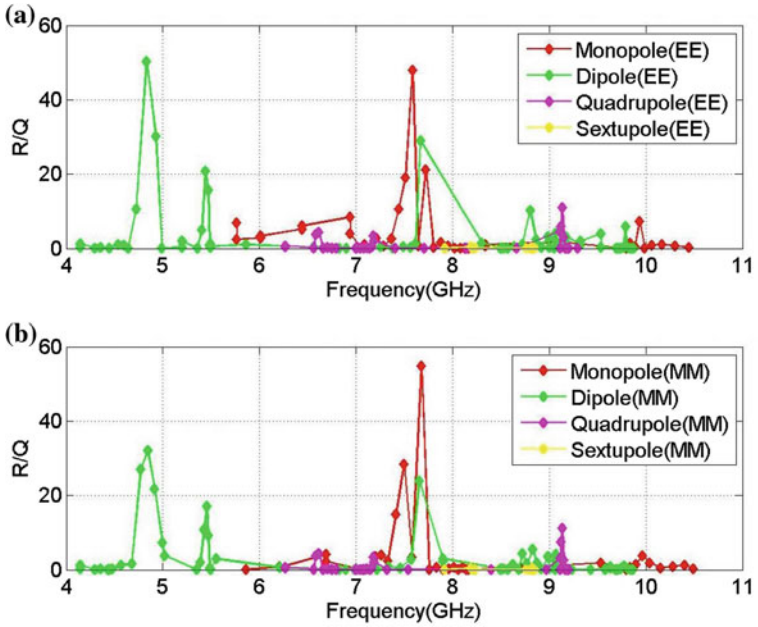

Fig. 2.11 The R/Q parameters of HOMs of a 9-cell third harmonic cavity versus the modal frequencies. The modes were calculated with electric (EE) boundaries and magnetic (MM) boundaries. The units of R/Q's are: Ω (monopole), Ω/cm^2 (dipole), Ω/cm^4 (quadrupole) and Ω/cm^6 (sextupole)

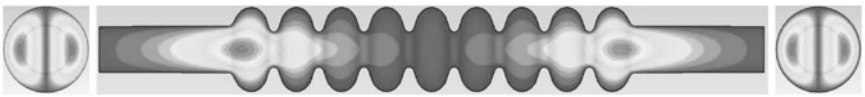

Fig. 2.12 The electric field distribution of one dipole beam-pipe mode (frequency: 4.1491 GHz, R/Q: 1.318 Ω/cm^2). Electric (EE) boundary conditions were used in the simulation. Reprinted with permission from [7]. Copyright 2012, American Institute of Physics

Fig. 2.13 The electric field distribution of one dipole beam-pipe mode (frequency: 4.1481 GHz, R/Q: 1.544 Ω/cm^2). Electric (EE) boundary conditions were used in the simulation

2.3 Eigenmodes of an Ideal Third Harmonic Cavity

The geometry of an ideal third harmonic cavity without couplers as modeled with CST Microwave Studio® [2] is shown in Fig. 2.5. The shape of an individual mid-cell is shown in Fig. 2.2a and the parameters are listed in Table 2.1. The end-cups have an

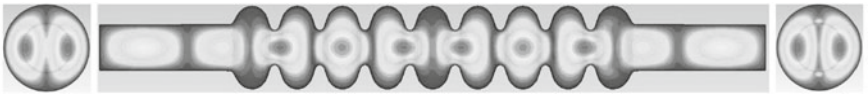

Fig. 2.14 The electric field distribution of one cavity mode from the first dipole band (frequency: 4.8327 GHz, R/Q: 50.307 Ω/cm^2). Electric (EE) boundary conditions were used in the simulation. Reprinted with permission from [7]. Copyright 2012, American Institute of Physics

Fig. 2.15 The electric field distribution of the strongest coupled cavity mode from the first dipole band (frequency: 4.8076 GHz, R/Q: 125.762 Ω/cm^2 per module). Electric (EE) boundary conditions were used in the simulation

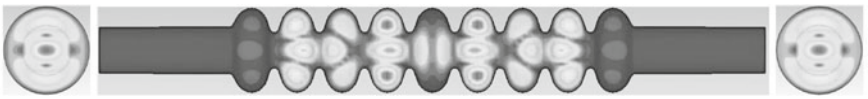

Fig. 2.16 The electric field distribution of one cavity mode from the fifth dipole band (frequency: 9.0581 GHz, R/Q: 2.171 Ω/cm^2). Electric (EE) boundary conditions were used in the simulation. Reprinted with permission from [7]. Copyright 2012, American Institute of Physics

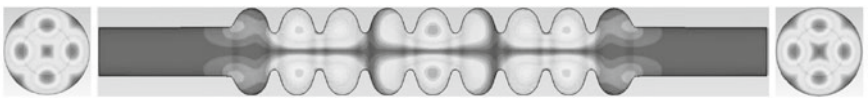

Fig. 2.17 The electric field distribution of one cavity mode from the first quadrupole band (frequency: 6.6167 GHz, R/Q: 4.358 Ω/cm^4). Electric (EE) boundary conditions were used in the simulation

increased iris radius (20 mm) and are connected with beam pipes at either ends. The simulations were conducted with Eigenmode Solver of CST Microwave Studio®. A solver accuracy of 10^{-6} in terms of the eigensystem's relative residual was used. The cavity geometry was approximated by hexahedral mesh cells. As shown in Fig. 2.6, the mesh lines were chosen such that the iris radius and the equator radius were exactly matched by mesh lines. A quarter of the structure with symmetry planes was used in order to reduce the simulation time. For the accelerating mode, a maximum mesh step of 1.1 mm, corresponding to approximately 2.1 million mesh cells for a quarter of the structure, was used. Electric (EE) boundary conditions were used both on the surface and the beam pipe ends.

The electric field of the accelerating mode (3.9 GHz, π mode [5]) is shown in Fig. 2.7a, b. The unit of R/Q is [Ω per cavity]. Throughout this report, R/Q is calculated "per cavity" and is often omitted from the unit unless explicitly otherwise stated. The longitudinal component of the electric field of the accelerating mode on the cavity axis is shown in Fig. 2.7c. The field flatness can be calculated as [6]

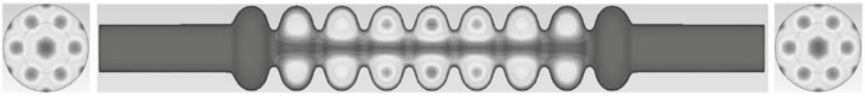

Fig. 2.18 The electric field distribution of one cavity mode from the first sextupole band (frequency: 8.1894 GHz, R/Q: 0.506 Ω/cm^6). Electric (EE) boundary conditions were used in the simulation

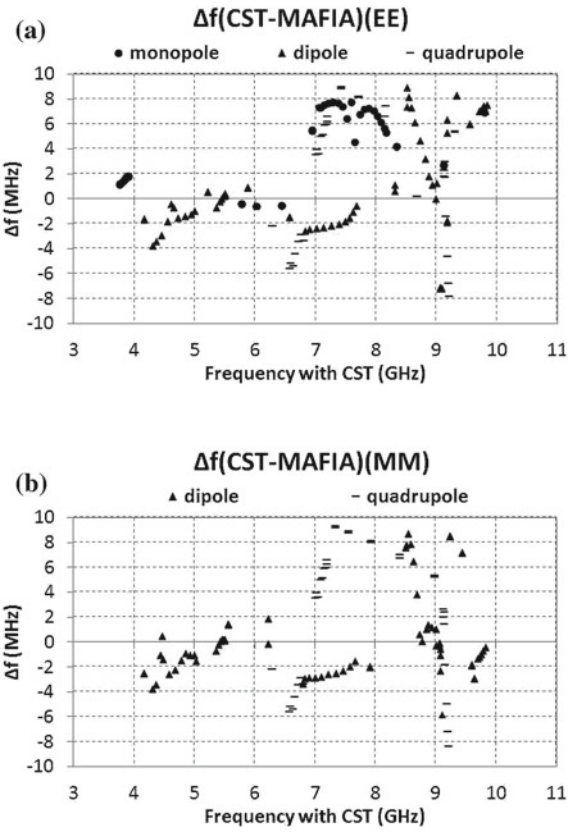

Fig. 2.19 Frequency differences of modes simulated with CST® and MAFIA®. Δf is calculated as $\Delta f = f_{CST} - f_{MAFIA}$

$$\text{field flatness} = \frac{(E_{cmax} - E_{cmin})}{\frac{1}{N}\sum_{i=1}^{N} E_{ci}} \times 100\,\%, \tag{2.5}$$

where E_{cmax} and E_{cmin} are the maximum and minimum peak axial electric fields in the multi-cell cavity, E_{ci} is the peak axial electric field in the i^{th} cell, N is the total number of cells in the cavity. In our case, $N = 9$. The field flatness is calculated to be 3.5 % for the accelerating mode.

The phase advance per cell can be calculated using the electric field determined from the simulations. Based on Eq. 2.1 for periodic structures, the phase advance per cell can be derived according to the Floquet periodicity conditions [4]:

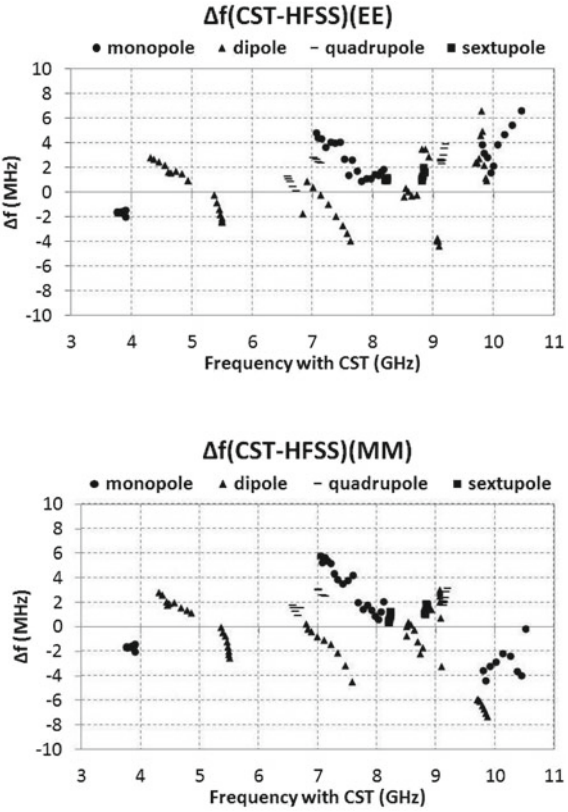

Fig. 2.20 Frequency differences of modes simulated with CST® and HFSS®. Δf is calculated as $\Delta f = f_{CST} - f_{HFSS}$

$$E_M = E_z(r, z), \tag{2.6}$$

$$E_L = E_M e^{-i\phi} = E_z(r, z - L), \tag{2.7}$$

$$E_R = E_M e^{i\phi} = E_z(r, z + L), \tag{2.8}$$

$$E_L + E_R = 2E_M cos(\phi), \tag{2.9}$$

where $E_z(r, z)$ is the longitudinal electric field obtained from the simulations, E_L, E_M and E_R are defined as illustrated in Fig. 2.8. The phase advance per cell can be calculated as

$$\phi = arccos\left(\frac{E_L + E_R}{2E_M}\right). \tag{2.10}$$

The phase advance per cell calculated in the middle of the cavity for the accelerating mode is 177 degrees. This reflects the field flattness that is adjusted by the geometry of the end-cells.

Equation 2.10 has been used to calculate the phase advance per cell for all modes which have been simulated. The results for monopole, dipole, quadrupole and sex-

tupole bands are shown in Fig. 2.9 along with dispersion curves of the mid-cell presented in Sect. 2.1. Beside the electric (EE) boundaries, another set of simulations with magnetic (MM) boundaries set on both beam pipe ends has also been presented. At both ends of the cavity, the longitudinal electric field is zero for the MM boundaries, while the transverse electric field is zero for the EE boundaries. These are used for the study of field distributions of the eigenmodes. The frequencies of the first monopole band are below the cutoff frequency of the beam pipe (see Table 2.3), therefore modes in this band do not depend on the boundary conditions. This can be seen in Fig. 2.9a as the overlap of asterisks and circles. Some dipole modes in the fifth dipole band and the first two modes in the first dipole band are trapped within the cavity, which explains the consistency of results from EE and MM boundary conditions in Fig. 2.9b. Large deviations for different boundary conditions can be clearly seen in other dipole bands as they are propagating amongst cavities. Figure 2.10a–d show the R/Q value versus the frequency of each mode for both EE and MM boundary conditions. The coupling strengths for all HOMs beyond the fundamental band are shown in Fig. 2.11a and b.

In addition to cavity modes shown in the bands, there are also beam-pipe modes, whose electromagnetic energy mainly deposits in beam pipes and end-cells of the cavity. These modes are trapped within both beam-pipe ends of the structure. One of these modes is shown in Fig. 2.12. The same mode has also been simulated with a structure shown in Fig. 2.13. The dipole character of this mode can be seen clearly in the projection on the transverse plane in the middle of each end-cell.

The propagating feature of one dipole cavity mode can be seen in Figs. 2.14 and 2.15. The mode can couple to adjacent cavities through attached beam pipes, and also has strong coupling to the beam represented by the large R/Q value.

One trapped cavity mode from the fifth dipole band is shown in Fig. 2.16. Compared with other trapped modes in this band, this mode has stronger coupling to the beam (larger R/Q value).

One quadrupole mode and one sextupole mode are also shown in Figs. 2.17 and 2.18. The R/Q values are in general small for these modes.

Compared to the eigenmode simulations obtained by using MAFIA® [8] and HFSS® [9], the frequencies of modes are shifted. A direct comparison between CST® and MAFIA® is shown in Fig. 2.19, while a comparison between CST® and HFSS® is shown in Fig. 2.20. The MAFIA® simulation results are from Ref. [1] while the HFSS® simulations are from Ref. [10]. The differences are within 10 MHz for both boundary conditions from both simulation codes. This is comparable to the frequency shift of HOMs in the real cavity from their eigenmode values due to asymmetric cavity structure caused by the couplers and fabrication tolerances. These are described in Chap. 3.

A list of simulated eigenmodes for an ideal third harmonic cavity is shown in Appendix B. The electric field distributions for the first monopole band, the first two dipole bands and the fifth dipole band are also shown in Appendix B for both electric (EE) and magnetic (MM) boundary conditions. Extensive electric field distributions for monopole, dipole, quadrupole and sextupole eigenmodes up to 10 GHz are described in Ref. [11] with both electric (EE) and magnetic (MM) boundary

conditions. Simulations of a four-cavity third harmonic module with couplers and beam-pipe bellows can be found in Ref. [12–16].

Having the knowledge of the band structure of the third harmonic 3.9 GHz cavity and field distributions of various modes from simulations, the experimental characterization of HOMs in the cavity/module both with and without beam-excitations are discussed in the Chap. 3.

References

1. T. Khabibouline et al., Higher order modes of a 3rd harmonic cavity with an increased end-cup Iris. TESLA-FEL Report: TESLA-FEL 2003-01 (2003)
2. C.S.T. Microwave, Studio®. Ver., CST AG, Darmstadt, Germany (2011)
3. D.M. Pozar, *Microwave Engineering*, third edn. Wiley, New York (2005)
4. R. Wanzenberg, Monopole, dipole and quadrupole passbands of the TESLA 9-cell cavity. TESLA Report: TESLA 2001-33 (2001)
5. J. Sekutowicz, R. Wanzenberg, W.F.O. Mueller, T. Weiland, A design of a 3rd harmonic cavity for the TTF 2 photoinjector. TESLA-FEL Report: TESLA-FEL 2002-05 (2002)
6. S. An, H. Wang, Tuner effect on the field flatness of SNS superconducting RF cavity. JLAB Note: JLAB-TN-03-043 (2003)
7. P. Zhang, N. Baboi, R.M. Jones, I.R.R. Shinton, T. Flisgen, H.W. Glock, A study of beam position diagnostics using beam-excited dipole modes in third harmonic superconducting accelerating cavities at a free-electron laser. Rev. Sci. Instrum. **83**, 085117 (2012)
8. MAFIA Release 4. CST AG, Darmstadt, Germany
9. ANSYS®HFSS. Release 11.2, ANSYS Inc., USA
10. I.R.R. Shinton et al., Compendium of eigenmodes in third harmonic cavities for FLASH and the XFEL. DESY Report: DESY 12-053 (2012)
11. P. Zhang, N. Baboi, R.M. Jones, Eigenmode simulations of third harmonic superconducting accelerating cavities for FLASH and the European XFEL. DESY Report: DESY 12-101 (2012)
12. I.R.R. Shinton et al., Higher order modes in third harmonic cavities for XFEL/FLASH, in *Proceedings of IPAC'10, (Kyoto, Japan)*, pp. 3007–3009 (2010)
13. I.R.R. Shinton et al., Higher order modes in third harmonic cavities at FLASH, in *Proceedings of Linear Accelerator Conference LINAC2010, (Tsukuba, Japan)*, pp. 785–787 (2010)
14. I.R.R. Shinton et al., Higher order modes in coupled cavities of the FLASH module ACC39, in *Proceedings of IPAC2011, (San Sebastian, Spain)*, pp. 2301–2303 (2011)
15. T. Flisgen et al., A concatenation scheme for the computation of beam excited higher order mode port signals, in *Proceedings of IPAC2011, (San Sebastian, Spain)*, pp. 2238–2240 (2011)
16. I.R.R. Shinton, R.M. Jones, Z. Li, P. Zhang, Simulations of higher order modes in the ACC39 module of FLASH, in *Proceedings of IPAC2012, (New Orleans, Louisiana, USA)*, pp. 1900–1902 (2012)

http://www.springer.com/978-3-319-00758-8

Beam Diagnostics in Superconducting Accelerating Cavities
The Extraction of Transverse Beam Position from Beam-Excited Higher Order Modes
Zhang, P.
2013, XII, 118 p. 180 illus., 40 illus. in color., Hardcover
ISBN: 978-3-319-00758-8